

Cite this article as: Wang Wensheng, Liu Xianghong, Wang Haipeng, et al. Characterization and Analysis of Abnormal Grain Structures in WSTi6421 Titanium Alloy After  $\beta$  Annealing Treatment[J]. Rare Metal Materials and Engineering, 2025, 54(02): 354-362. <https://doi.org/10.12442/j.issn.1002-185X.20240016>.

ARTICLE

# Characterization and Analysis of Abnormal Grain Structures in WSTi6421 Titanium Alloy After $\beta$ Annealing Treatment

Wang Wensheng<sup>1,2</sup>, Liu Xianghong<sup>2</sup>, Wang Haipeng<sup>1</sup>, Wang Kaixuan<sup>2</sup>, Tian Yanwen<sup>2</sup>, Yan Jianchuan<sup>2</sup>, Li Yulu<sup>2</sup>, Chen Haisheng<sup>2</sup>

<sup>1</sup> Northwestern Polytechnical University, Xi'an 710072, China; <sup>2</sup> Western Superconducting Technologies Co., Ltd, Xi'an 710018, China

**Abstract:** As-forged WSTi6421 titanium alloy billet after  $\beta$  annealing was investigated. Abnormally coarse grains larger than adjacent grains could be observed in the microstructures, forming abnormal grain structures with uneven size distribution. Through electron backscattered diffraction (EBSD), the forged microstructure at various locations of as-forged WSTi6421 titanium alloy billet was analyzed, revealing that the strength of the  $\beta$  phase cubic texture generated by forging significantly influences the grain size after  $\beta$  annealing. Heat treatment experiments were conducted within the temperature range from  $T_{\beta}-50$  °C to  $T_{\beta}+10$  °C to observe the macro- and micro-morphologies. Results show that the cubic texture of  $\beta$  phase caused by forging impacts the texture of the secondary  $\alpha$  phase, which subsequently influences the  $\beta$  phase formed during the post- $\beta$  annealing process. Moreover, the pinning effect of the residual primary  $\alpha$  phase plays a crucial role in the growth of  $\beta$  grains during the  $\beta$  annealing process. EBSD analysis results suggest that the strength of  $\beta$  phase with cubic texture formed during forging process impacts the orientation distribution differences of  $\beta$  grains after  $\beta$  annealing. Additionally, the development of grains with large orientations within the cubic texture shows a certain degree of selectivity during  $\beta$  annealing, which is affected by various factors, including the pinning effect of the primary  $\alpha$  phase, the strength of the matrix cubic texture, and the orientation relationship between  $\beta$  grain and matrix. Comprehensively, the stronger the texture in a certain region, the less likely the large misoriented grains suffering secondary growth, thereby aggregating the difference in microstructure and grain orientation distribution across different regions after  $\beta$  annealing.

**Key words:** WSTi6421 titanium alloy;  $\beta$  annealing; abnormal grain structure

Damage-tolerant titanium alloys have been extensively used in the aerospace industry because of their outstanding fracture toughness and resistance against fatigue crack propagation<sup>[1-5]</sup>. To improve the damage tolerance of titanium alloys, it is customary to perform the  $\beta$  annealing process. The annealing temperature is usually set between  $T_{\beta}+10$  °C and  $T_{\beta}+50$  °C with the holding time exceeding 30 min<sup>[6]</sup>. To achieve a uniform grain distribution in the microstructure, it is essential to precisely control the  $\beta$  annealing parameters<sup>[7-8]</sup>. Typically, the grain size distribution of the material after  $\beta$  annealing follows a normal distribution. However, some materials exhibit the bimodal distribution of grain sizes after  $\beta$  annealing, resulting in the abnormal grain structure (AGS)<sup>[9]</sup>,

which severely impacts the mechanical properties of the products.

Generally, the formation mechanism of AGS is considered as the discontinuous or abnormal growth of the original  $\beta$  grains<sup>[10-14]</sup>. However, the deformation textures with strong orientation can induce abnormal grain growth<sup>[10]</sup>. Pilchak et al<sup>[12]</sup> even suggested that AGS is closely linked to the texture changes during the recrystallization process. Therefore, the AGS formation mechanism remains obscure. In this research, a novel damage-tolerant titanium alloy WSTi6421 was used for investigation, which was independently developed by Western Superconducting Technologies Co., Ltd<sup>[12,15-16]</sup>. The microstructure at various locations of the forging was

Received date: January 09, 2024

Foundation item: Key Research and Development Plan of Shaanxi Province (2023-YBGY-493)

Corresponding author: Liu Xianghong, Ph. D., Professor, Western Superconducting Technologies Co., Ltd, Xi'an 710018, P. R. China, Tel: 0086-29-86514523, E-mail: wwsawy@163.com

Copyright © 2024, Northwest Institute for Nonferrous Metal Research. Published by Science Press. All rights reserved.

analyzed. The evolution of  $\beta$  grains during heat treatment and the factors influencing the AGS formation were discussed, providing research guidance for the AGS formation process in titanium alloys.

## 1 Experiment

The experiment material supplied by Western Superconductor Materials Technology Co., Ltd is a forged billet of WSTi6421 titanium alloy, as shown in Fig. 1. The chemical composition of WSTi6421 titanium alloy was Ti-6Al-4Mo-2Zr-1Nb. The longitudinal (L), longitudinal-transverse (LT), and short-transverse (ST) orientations of billet were defined for further description and analysis. After approximately 70% forging deformation, the WSTi6421 titanium alloy ingot was transformed into a billet with L×LT×ST dimension of 500 mm×450 mm×150 mm. The  $\beta$  phase transition temperature is 970 °C.

As shown in Fig.1, the sample with thickness of 30 mm was extracted from the central region along L direction of the billet and subsequently bisected along LT direction into two equal portions. One segment underwent  $\beta$  annealing at 980 °C for 30

min followed by air cooling, whereas the other segment remained original forged state for comparison. Afterwards, both segments were subjected to etching using the mixed solution of H<sub>2</sub>O:HNO<sub>3</sub>:HF=16:3:1. As illustrated in Fig. 1, the samples were retrieved from the surface region, quarter thickness region, and center region of the  $\beta$ -annealed sample to analyze the microstructure at different depths. Similarly, samples were also obtained from the as-forged one at the same regions for electron backscattered diffraction (EBSD) analysis. To investigate the  $\beta$ -annealed microstructure evolution, five samples with L×LT×ST dimension of 10 mm×10 mm×30 mm were extracted from the blue area indicated in Fig. 1b through electric discharge wire cutting. The samples underwent heat treatment at temperatures of 920, 940, 960, 970, and 980 °C with the heating rate of 5 °C/min and held at the designed temperature for 30 min before air cooling. The samples were then polished and etched with the mixed solution for both macrostructure and microstructure examination. Before EBSD analysis, the samples were electropolished using the mixture of glacial acetic acid: perchloric acid=10: 1. EBSD experiments were performed by field emission scanning electron microscope (SEM, JSM-IT700HR) equipped with EBSD data collection system. The operation voltage was 20 kV, the scanning distance was 19 mm, and the step size was 1–2  $\mu$ m. Aztec Crystal software was used to process the experiment data.

## 2 Results and Discussion

### 2.1 AGS macrostructure

The macrostructures of  $\beta$ -annealed samples are shown in Fig. 2a. Abnormal coarse grains (ACGs) can be observed in the  $\beta$ -annealed samples without any surrounding distinct grain structure. Fig. 2b–2c illustrate the uniform  $\beta$ -recrystallized structures on the surface and at the quarter thickness region of the  $\beta$ -annealed sample, whose grain sizes range from 0.5 mm to 1.0 mm. As highlighted by the dotted areas in Fig. 2a, ACGs with 2–4 mm in size are located among the fine grains in the center region.

### 2.2 Characterization and analysis of forged microstructures

The orientation distribution maps of the surface region, quarter thickness region, and center region of the as-forged

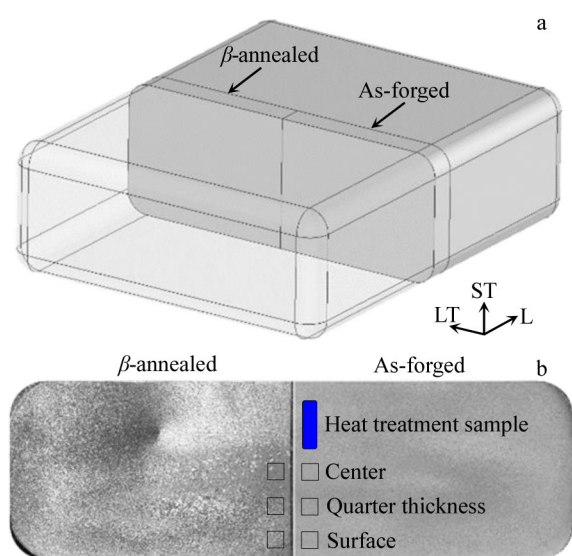


Fig.1 Schematic diagram (a) and appearance (b) of sampling locations and reference coordinate system for  $\beta$ -annealed and as-forged samples

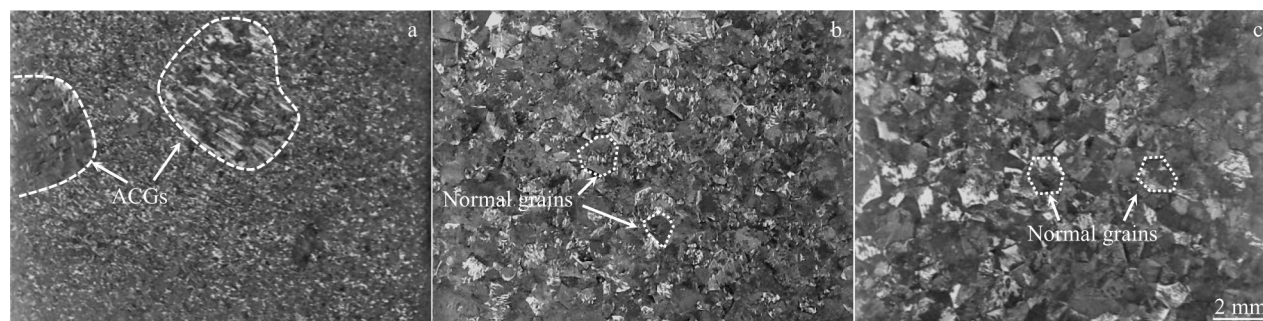


Fig.2 Macrostructures at center region (a), quarter thickness region (b), and surface region (c) of  $\beta$ -annealed sample

sample are shown in Fig.3, as well as the pole figures of  $\alpha$  and  $\beta$  phases. EBSD observation area is  $3000\ \mu\text{m}\times 2000\ \mu\text{m}$ , the inside microstructures are uniform, so the section of  $1000\ \mu\text{m}\times 500\ \mu\text{m}$  is selected to illustrate the orientation distribution. The pole densities of  $\alpha$  phase and transformed  $\beta$  phase (1%–2%) are identified with scan step size of  $1.25\ \mu\text{m}$ , which exhibit an increasing trend from the surface towards the center region. As shown in Fig.3c and 3i, the orientation distribution of  $\alpha$  phase in the center region shows obvious textures (green and purple-red) with strong symmetry. The textures on L-LT plane of  $\{0001\}$  pole figure (maximum  $0.84^\circ$ ) and those parallel to ST direction of  $\{11\bar{2}0\}$  pole figure (maximum  $0.50^\circ$ ) can be observed. As shown in Fig. 3f, the  $\beta$  phase orientation distribution of the center region is predominantly  $[100]$ -oriented (red). Combined with Fig. 3l, the  $\beta$  phase texture is the  $\{100\}\langle 100\rangle$  cubic texture (maximum  $1.34^\circ$ ) in  $\{001\}$  pole figure. Fig. 3b, 3e, 3h, and 3k show the  $\alpha$  and  $\beta$  phase orientation distributions and pole figures of the quarter thickness region in the as-forged sample. The symmetry degree and pole densities of the quarter thickness region are lower than those of the center region. As shown in Fig.3a, 3d,

3g, and 3j, no strong textures can be observed on the surface region.

Orientation distribution functions (ODFs) of the cross-sections of  $\alpha$  phase at  $\varphi_2=0^\circ$  and  $\varphi_2=30^\circ$  based on the Bunge-Euler angles ( $\varphi_1, \Phi, \varphi_2$ ) are shown in Fig. 4a. Two types of orientation density extremes with different textures appear in the cross-sections. When  $\varphi_2=0^\circ$ , the orientation density extreme appears at  $(45^\circ, 90^\circ, 0^\circ)$ ; when  $\varphi_2=30^\circ$ , the strong orientation density extremes appear at  $(0^\circ, 45^\circ, 30^\circ)$  and  $(90^\circ, 45^\circ, 30^\circ)$ . Combining the symmetry characteristics of pole figure of  $\alpha$  phase, schematic diagrams of the abovementioned Bunge-Euler orientations of  $\alpha$  grains in the as-forged sample and their positions in the  $\{0001\}$  pole figures are shown in Fig. 4b. The grains are rendered according to ST direction of inverse pole figure (IPF) color scale. Based on the spatial distribution characteristics of grains, three strongly oriented  $\alpha$  phases and the residual cubic  $\beta$  phase have Burgers orientation relationships of  $\{0001\}_\alpha\parallel\{110\}_\beta$  and  $\langle 11\bar{2}0\rangle_\alpha\parallel\langle 111\rangle_\beta$ . Through geometric relationship conversion, the texture orientation at  $\varphi_2=0^\circ$  is  $\langle 11\bar{2}0\rangle\parallel\text{ST}$  ( $\Delta=0^\circ$ ) in ODF diagram, and that at  $\varphi_2=30^\circ$  is  $\langle 60\bar{6}7\rangle\parallel\text{ST}$  ( $\Delta\approx 8^\circ$ ). The

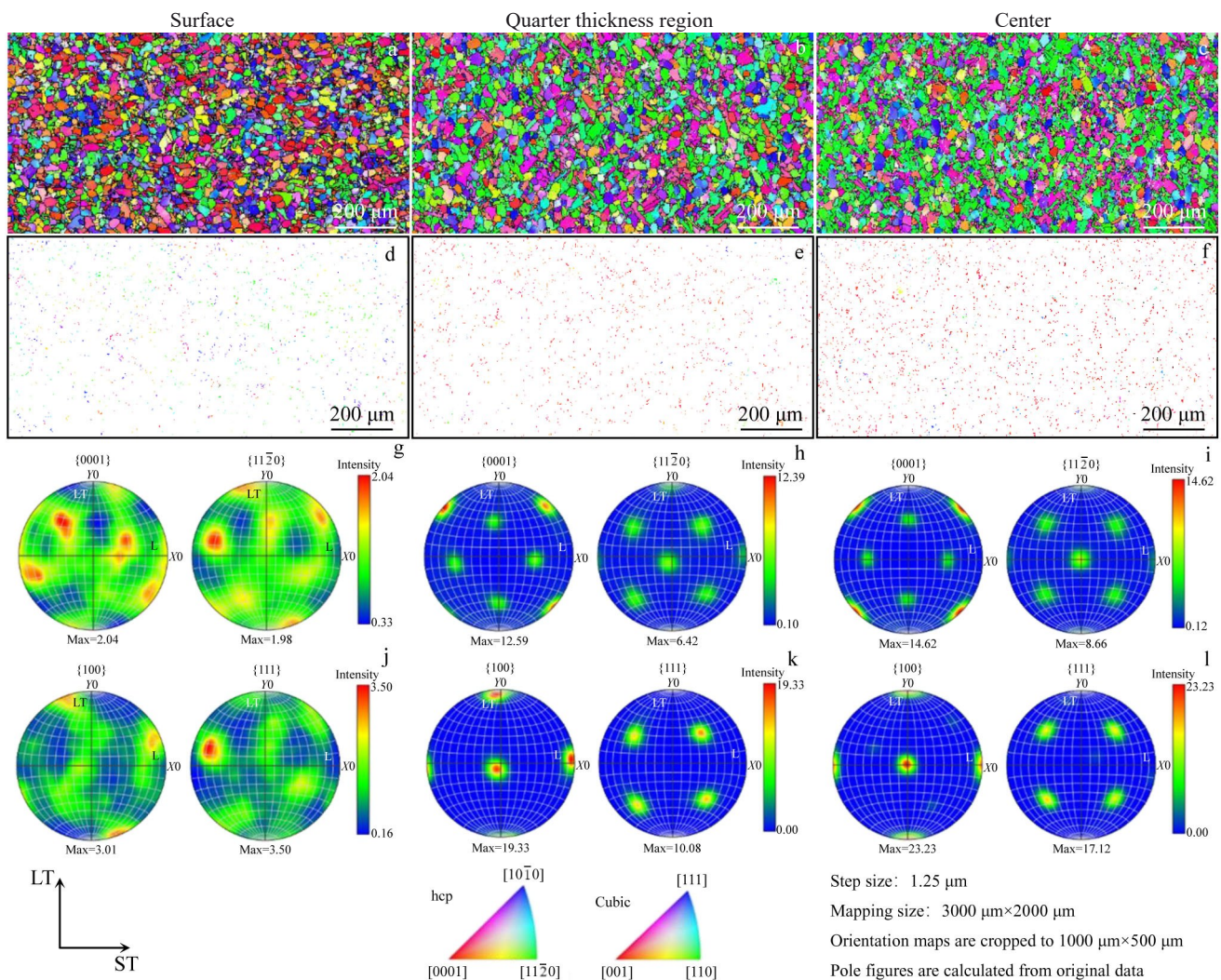


Fig.3 Orientation distributions (a–f) and pole figures (g–l) of  $\alpha$  phase (a–c, g–i) and  $\beta$  phase (d–f, j–l) at different locations of as-forged samples: (a, d, g, j) surface region, (b, e, h, k) quarter thickness region, and (c, f, i, l) center region

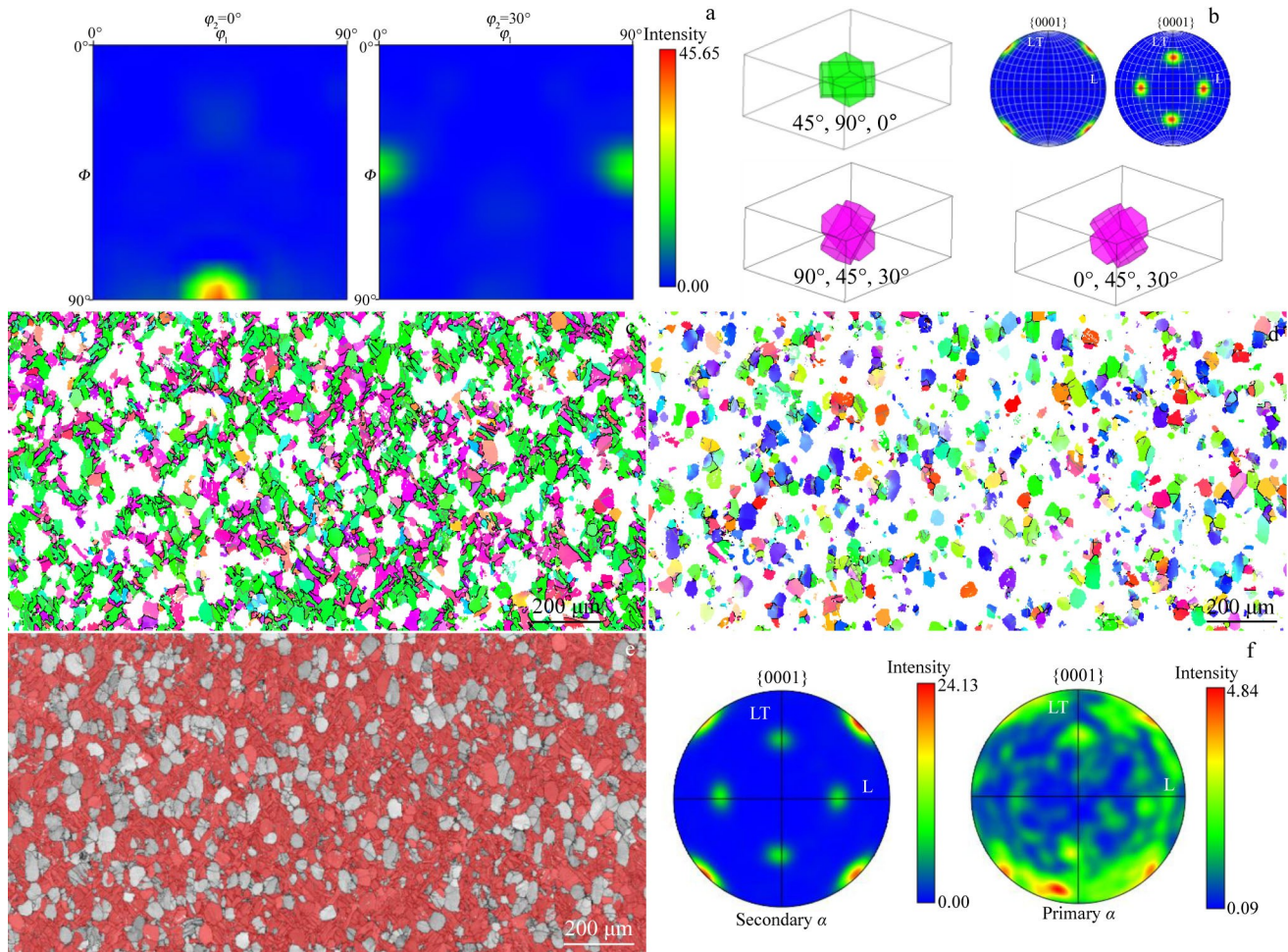


Fig.4 Microstructure analyses of  $\alpha$  phase in center region of as-forged samples: (a) ODF cross-section views and orientation density extremum; (b) schematic diagrams of grain distribution of orientation density extremes; (c) IPF of orientation density extreme; (d) IPF of residual components; (e) comparison of orientation density extremes with band contrast map; (f) pole figures of the regions in Fig.4c and 4d

components along  $\langle 11\bar{2}0 \rangle$  and  $\langle 60\bar{6}7 \rangle$  directions deviating from ST direction by less than  $15^\circ$  are shown in Fig.4c, which are mainly composed of lamellar  $\alpha$  (secondary  $\alpha$ ) phase. The white parts deviate from ST direction by more than  $15^\circ$ , as shown in Fig.4d, which are mainly the spherical  $\alpha$  (primary  $\alpha$ ) phase. The components in Fig.4c are marked in red for the comparison with band contrast map, as shown in Fig.4e, and the pole figures of secondary  $\alpha$  and primary  $\alpha$  phases are shown in Fig.4f. It is found that the  $\alpha$  phase texture mainly originates from the lamellar secondary  $\alpha$  phase.

In summary, the cubic texture of the  $\alpha$  phase predominantly appears in the secondary  $\alpha$  phase and it is associated with the Burgers orientation relationship with the residual  $\beta$  phase cubic texture. This result suggests that the  $\beta$  phase in the center region develops a cubic texture during forging. At the center region, the texture strength is higher, and AGS forms after  $\beta$  annealing. Conversely, at the quarter thickness region, the texture strength is lower, and AGS does not form after  $\beta$  annealing. This indicates that the strength of the cubic texture caused by  $\beta$  phase during forging significantly influences the microstructures after  $\beta$  annealing.

### 2.3 Heat treatment and microstructure evolution

The macrostructures of the samples after  $\beta$  annealing at 920, 940, 960, 970, and 980  $^\circ\text{C}$  are shown in Fig. 5. After  $\beta$  annealing at 920 and 940  $^\circ\text{C}$ , visible  $\beta$  grains hardly exist in any region. However, after  $\beta$  annealing at 960  $^\circ\text{C}$ , the macrostructures vary across different regions. Several  $\beta$  recrystallized grains ranging from 100  $\mu\text{m}$  to 500  $\mu\text{m}$  emerge near the surface region. After  $\beta$  annealing at 970  $^\circ\text{C}$  ( $\beta$ -transus temperature), significant transformation can be observed in the macrostructures of all regions, which is characterized by the formation of  $\beta$  grains with 1.0–1.6 mm in size in the surface region and a few large independent  $\beta$  grains in other areas. After  $\beta$  annealing at 980  $^\circ\text{C}$ , the  $\beta$  grains near surface expand, whereas the macrostructures near the center region are still similar to those after  $\beta$  annealing at 970  $^\circ\text{C}$ .

Fig. 6 shows the schematic diagram of sampling positions for microstructure observation of samples after  $\beta$  annealing at different temperatures. Accordingly, SEM microstructures at different positions of the as-forged and annealed samples are shown in Fig. 7. Position A, B, and C denote three equidistant analysis spots from the top to the bottom of the samples. After

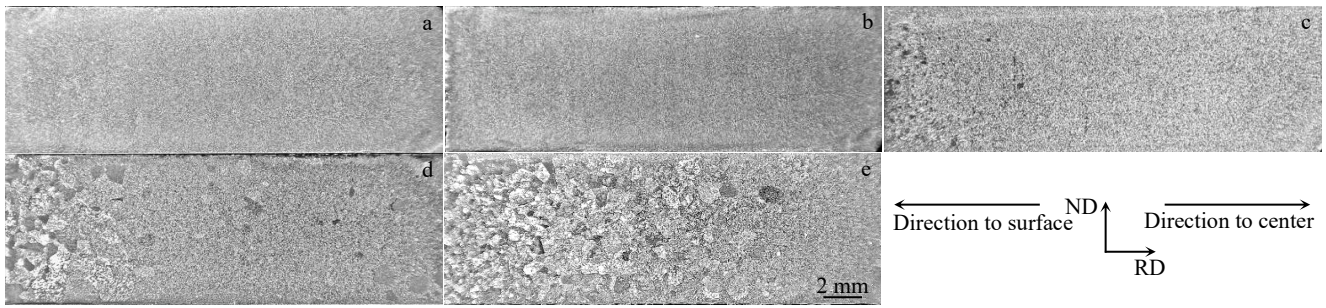


Fig.5 Macrostructures of samples after  $\beta$  annealing at different temperatures: (a) 920 °C, (b) 940 °C, (c) 960 °C, (d) 970 °C, and (e) 980 °C

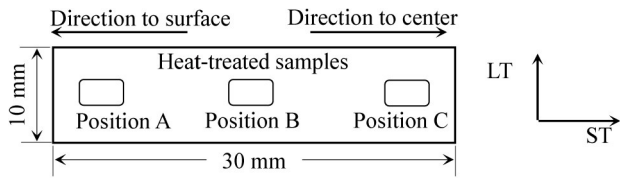


Fig.6 Schematic diagram of sampling positions for microstructure observation of samples after  $\beta$  annealing at different temperatures

$\beta$  annealing at 920 and 940 °C, the microstructures at all positions are consistent. Fig.7a–7c display the microstructures at position A of the samples before (as-forged) and after  $\beta$  annealing at 920 and 940 °C. The forged microstructure

presents a bimodal structure. After  $\beta$  annealing at 920 °C, the size and distribution of primary  $\alpha$  phase within the microstructure barely change, compared with those of the forged sample. The secondary  $\alpha$  phase changes slightly and a significant transformation into the transformed  $\beta$  phase can be observed, as indicated by the gray area in Fig.7b. After  $\beta$  annealing at 940 °C, the primary  $\alpha$  phase decreases, and the  $\beta$  grain boundaries are pinned by the residual primary  $\alpha$  phase, as denoted by the arrows in Fig.7c. The microstructures at position A, B, and C of the samples annealed at 960 °C are illustrated in Fig.7d–7f, respectively. Each region contains approximately 8% primary  $\alpha$  phase. As indicated by the dashed area in Fig.7d, large  $\beta$  grains are not pinned by the residual primary  $\alpha$  phase at position A, so the  $\beta$  grain sizes

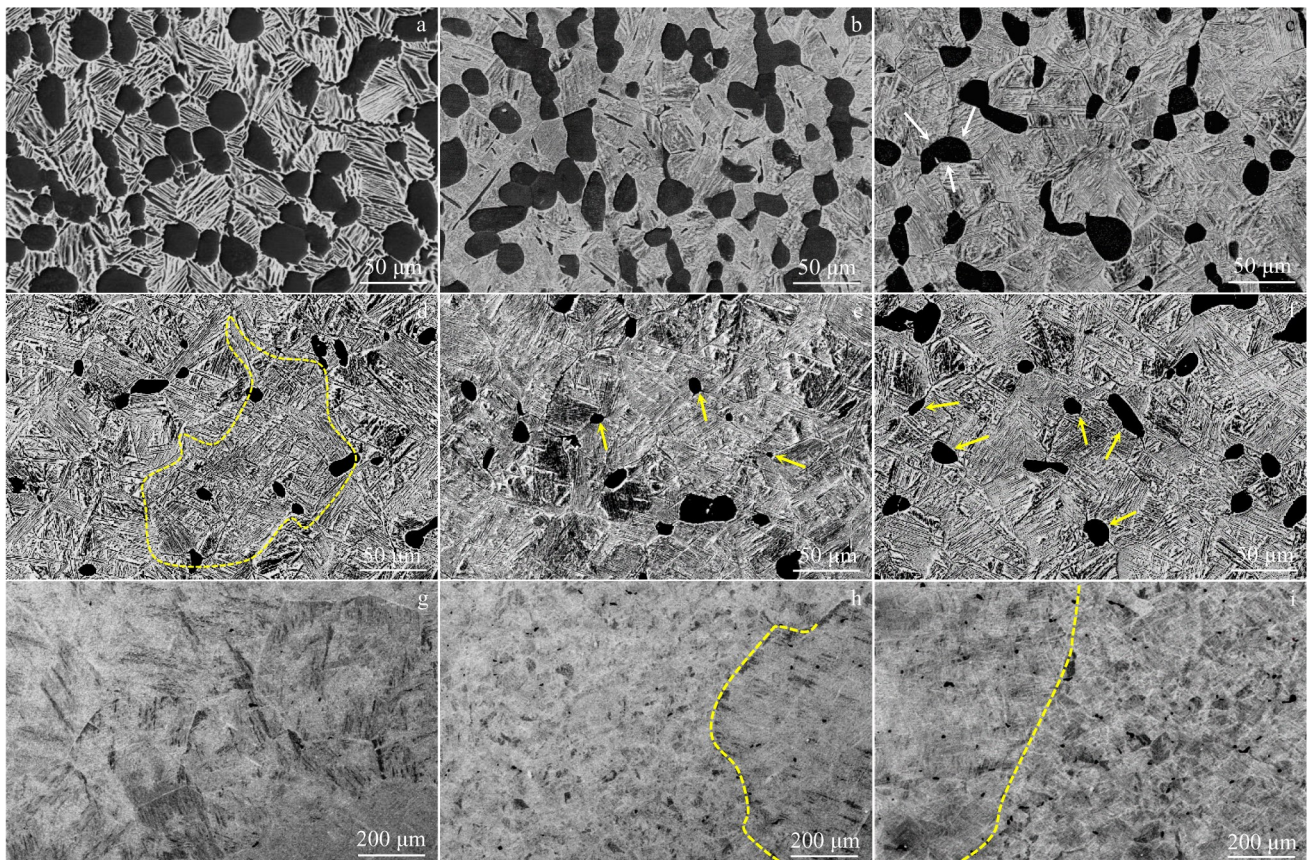


Fig.7 SEM microstructures at position A (a–d, g), position B (e, h), and position C (f, i) of samples after  $\beta$  annealing at different temperatures: (a) as-forged; (b) 920 °C; (c) 940 °C; (d–f) 960 °C; (g–i) 970 °C

reach about 100  $\mu\text{m}$ . However, at position B and C, the  $\beta$  grain boundaries are pinned by the residual primary  $\alpha$  phase, as indicated by the arrows in Fig. 7e–7f. Fig. 7g–7i present the microstructures at position A, B, and C of the samples annealed at 970  $^{\circ}\text{C}$ . It can be seen that the position A is mainly composed of  $\beta$  grains, and position B and C consist of millimeter-sized  $\beta$  grains amidst the fine  $\beta$  grains, as indicated by the dashed lines in Fig. 7h–7i.

In summary, with the increase in the heat treatment ( $\beta$  annealing) temperature, the transformation of  $\alpha$  phase occurs in two stages. Initially, the secondary  $\alpha$  phase is transformed, leading to the early formation of the  $\beta$  phase during heat treatment. Subsequently, the primary  $\alpha$  phase is transformed, during which the  $\alpha$  phase size progressively decreases. At this juncture, the remaining primary  $\alpha$  phase serves as the secondary phase, pinning the  $\beta$  grain boundaries. Near the surface region of as-forged sample, the  $\beta$  grains can more easily overcome the pinning effect of the residual primary  $\alpha$  phase and grow rapidly at the temperatures between 960 and 970  $^{\circ}\text{C}$ . Near the center region of as-forged sample, higher temperatures are necessary for the  $\beta$  grain growth, resulting in the less formation of  $\beta$  grains and the macrostructure variation of the annealed samples.

Applying the Burgers orientation correlation, the  $\beta$  phase subjected to annealing at 940, 960, and 980  $^{\circ}\text{C}$  is meticulously reconstructed. EBSD orientation distributions and quality distributions of the  $\beta$  phase at position A, B, and C in samples

annealed at 940 and 960  $^{\circ}\text{C}$  are shown in Fig. 8<sup>[6]</sup>. It can be seen that spherical white spots represent the residual primary  $\alpha$  phase. Importantly, some residual primary  $\alpha$  phases contribute to the reconstruction of  $\beta$  phase, so  $\beta$  grains with significant misorientation can be observed, potentially complicating the analysis of  $\beta$  grain evolution. The primary  $\alpha$  phase can be easily identified owing to its robust structural integrity. After  $\beta$  annealing at 980  $^{\circ}\text{C}$ , four typical locations for EBSD analysis are selected and marked in Fig. 9a. Further analysis in  $\beta$  phase reconfiguration orientation distributions and grain boundary misorientations is also conducted.

As depicted in Fig. 8, after  $\beta$  annealing at 940 and 960  $^{\circ}\text{C}$ , the cubic texture of  $\beta$  phase predominates at all three positions, and most  $\beta$  grains are delineated by low-angle grain boundaries (misorientation of  $3^{\circ} - 15^{\circ}$ ), thereby forming  $\beta$  subgrains, namely the matrix. The intensity of the cubic texture is increased at all positions with the increase in  $\beta$  annealing temperature. As shown in Fig. 8a – 8c, after  $\beta$  annealing at 940  $^{\circ}\text{C}$ , the quantity of high-angle  $\beta$  grains diminishes from position A to position C, which is attributed to the pinning effect of the residual primary  $\alpha$  phase, thereby hindering significant size disparities of  $\beta$  grains. After  $\beta$  annealing at 960  $^{\circ}\text{C}$ , three changes can be observed in the orientation distribution of  $\beta$  phase at position A. Firstly, as indicated by the arrows in Fig. 8d, the high-angle  $\beta$  grains near the  $[110]$  orientation (green), which commonly exist after annealing at 940  $^{\circ}\text{C}$ , completely vanish, implying that these

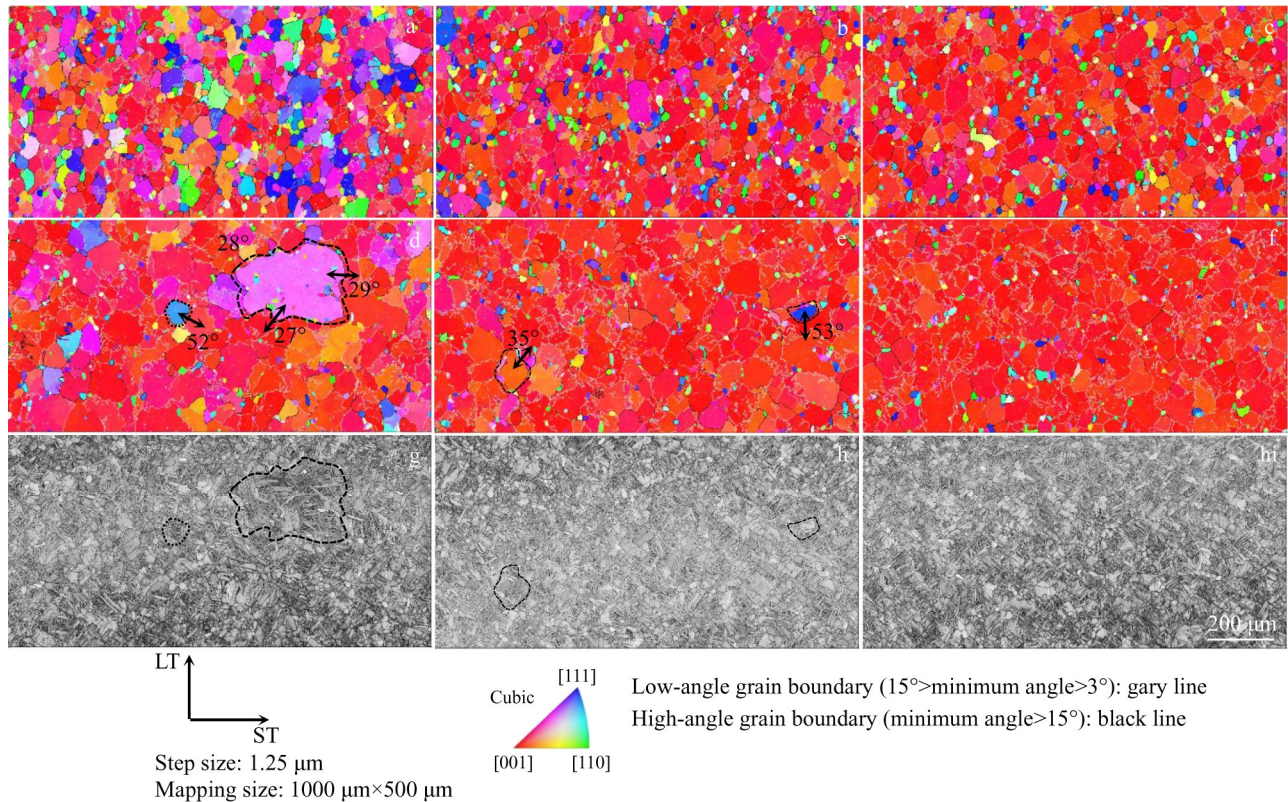


Fig.8 EBSD orientation distributions (a–f) and quality distributions (g–i) of  $\beta$  phase reconstruction at position A (a, d, g), position B (b, e, h), and position C (c, f, i) of samples after annealing at 940  $^{\circ}\text{C}$  (a–c) and 960  $^{\circ}\text{C}$  (d–i)

grains are the first ones undergoing transformation. Secondly, as illustrated by the dashed areas in Fig. 8d,  $\beta$  grains manage to grow despite the pinning effect of residual primary  $\alpha$  phase, exhibiting a misorientation of approximately  $28^\circ$  from the matrix and thereby gaining a size advantage and the potential for the further growth with the increase in heat treatment temperature. Thirdly, multiple high-angle  $\beta$  grains near the [111] orientation (blue) are detected with a misorientation of about  $52^\circ$  from the matrix, whose size is comparable to that of  $\beta$  subgrains. Additionally, these  $\beta$  grains can suffer secondary growth with the increase in heat treatment temperature. At position B, as depicted by the dashed areas in Fig. 8e, the high-angle grains with a misorientation of about  $35^\circ$  from the

matrix exhibit a tendency to grow, overcoming the pinning effect of the residual primary  $\alpha$  phase. The grains near the [111] orientation (blue) in Fig. 8e with a misorientation of about  $53^\circ$  from the matrix are markedly smaller than the adjacent  $\beta$  subgrains, and with the increase in heat treatment temperature, these grains are more likely to be assimilated by the matrix. As demonstrated in Fig. 8f, the cubic texture at position C is the most pronounced with only occasional high-angle grain boundaries emerging within the matrix and no complete high-angle  $\beta$  grains can be observed.

As shown in Fig. 9b–9e, after  $\beta$  annealing at  $980^\circ\text{C}$ , there is a noticeable decline in both the number of large-sized  $\beta$  grains and the misorientation in four distinct locations. At location I

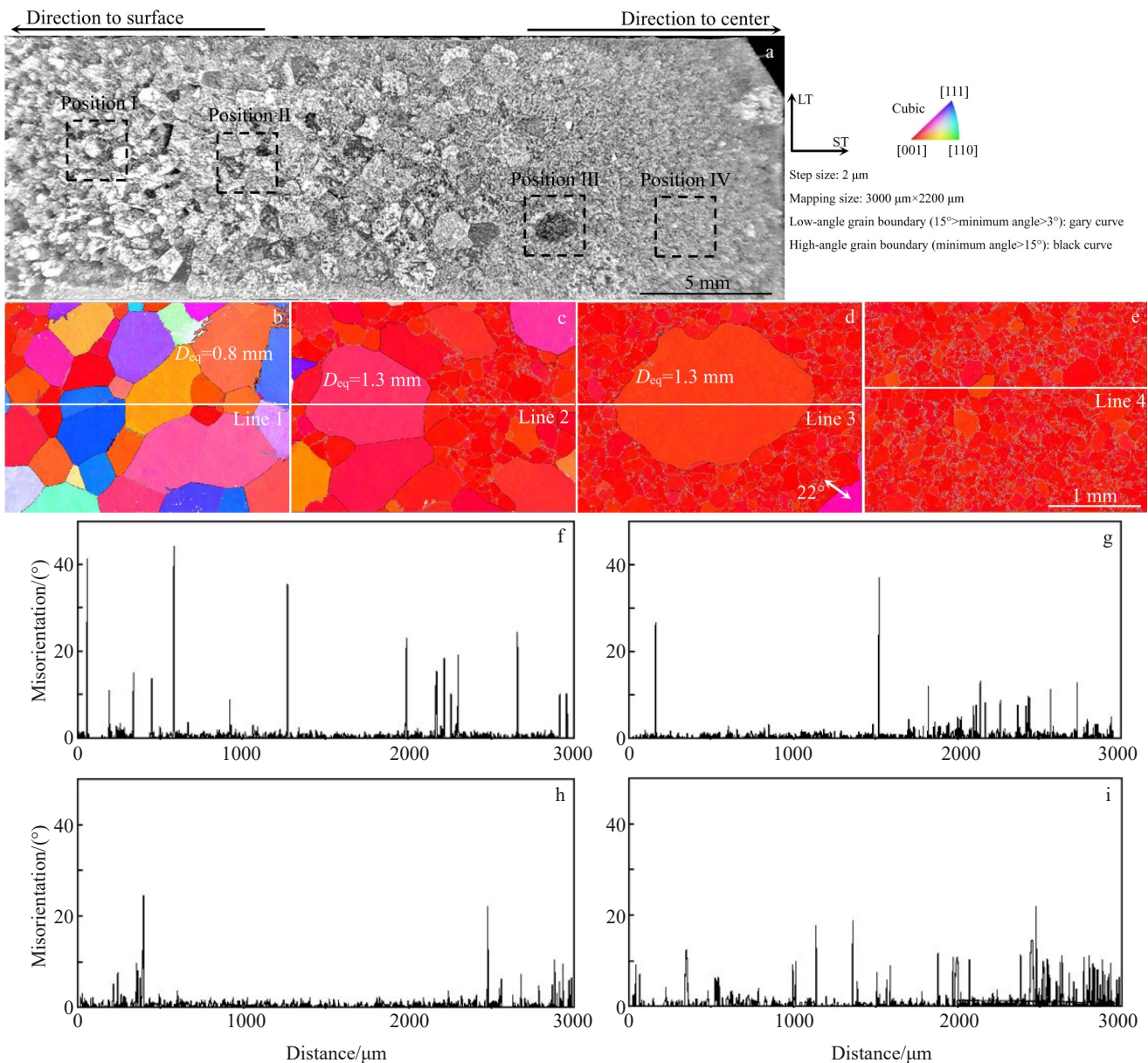


Fig.9 Macrostructure of sample after annealing at  $980^\circ\text{C}$  (a);  $\beta$  phase reconfiguration orientation distributions of position I (b), position II (c), position III (d), and position IV (e) in Fig. 9a; grain boundary misorientations along Line 1 (f), Line 2 (g), Line 3 (h), and Line 4 (i) in Fig. 9b–9e, respectively

(equivalent to position A),  $\beta$  grains of uniform size are detected with the majority of their orientations ranging between [001] and [111]. This suggests that some large-angle  $\beta$  grains near the [111] orientation (blue) after  $\beta$  annealing at 960 °C undergo secondary growth with the increase in heat treatment temperature. Location II is characterized as a transitional area with varying  $\beta$  annealing structures, where the misorientation between  $\beta$  grains and the cubic texture matrix is markedly smaller than that at location I. The largest grain (equivalent diameter of 1.8 mm) displays a misorientation of about 38° from the  $\beta$  matrix. Location III exhibits a typical ACG structure, where isolated large-sized grains (equivalent diameter of 2.3 mm) can be detected with a misorientation of approximately 22° from the matrix. Location IV is composed of the matrix of fine  $\beta$  grains. At location IV, the sizes of large-angle  $\beta$  grains are similar to those of  $\beta$  subgrains, and the misorientation is 19° from the matrix. No distinct  $\beta$  grains can be observed at location IV.

After  $\beta$  annealing at 980 °C, it is noted that the misorientation of  $\beta$  grains formed near the center region is smaller and the grains reduce, signifying a macrostructural change. This variation is attributed to the cubic texture generated during the forging process. After  $\beta$  annealing, the center region exhibits a markedly small number of high-angle grains and small misorientation, compared with those of other regions. Consequently, the strength of the  $\beta$  phase cubic texture formed during forging plays a crucial role in the development of  $\beta$  annealing structures. Theoretically, when the size of the high-angle  $\beta$  grains approaches that of the  $\beta$  subgrains in the matrix, the misorientation increases, which increases the grain boundary migration energy, facilitating the absorption during heat treatment. Therefore, the strength of the cubic texture is intensified with the increase in heat treatment temperature. This phenomenon aligns with the theoretical predictions. However, experiment data suggest that the growth of large orientation grains within the cubic texture is selective. It is influenced by various factors, such as the pinning effect of the primary  $\alpha$  phase, the cubic texture strength in the matrix, and the orientation relationship between the  $\beta$  grains and the matrix. Some  $\beta$  grains with smaller misorientation manage to overcome the pinning effect, thereby gaining a size advantage within the matrix.  $\beta$  grains oriented closely to [110] are the most likely to be assimilated by the matrix, and with the increase in cubic texture strength,  $\beta$  grains near [111] orientation are also prone to assimilation. Consequently, the development of AGS near the center region after  $\beta$  annealing can be characterized by not only the texture strength but also the diminished survival ratio of large misorientation  $\beta$  grains within the strong cubic texture, thereby amplifying the disparities in structure and grain orientation distribution in different regions after  $\beta$  annealing.

### 3 Conclusions

1) In the  $\beta$ -annealed microstructure, ACGs with sizes significantly larger than those of surrounding grains can be observed, particularly in the center region along ST direction. These ACGs are interspersed among fine grains, forming AGS.

2) The formation of  $\beta$  phase during forging is a prerequisite for the development of AGS, and the strength of the cubic texture affects the evolution process of the  $\beta$ -annealed structure.

3) During the phase transformation process, the cubic texture of the  $\beta$  phase produced during forging is inherited initially by the secondary  $\alpha$  phase and subsequently by the newly formed  $\beta$  phase. The cubic texture of the  $\beta$  phase produced during forging is essential for the formation of AGS, and texture strength influences the microstructures after  $\beta$  annealing.

### References

- 1 Guo P, Zhao Y Q, Zeng W D et al. *Materials Science and Engineering A*[J], 2013, 563: 106
- 2 Lu W, Shi Y W, Lei Y P et al. *Materials & Design*[J], 2012, 34: 509
- 3 Feng B X, Mao X N, Yang G J et al. *Materials Science and Engineering A*[J], 2009, 512: 105
- 4 Zhao Q Y, Chen Y N, Xu Y K et al. *Rare Metal Materials and Engineering*[J], 2020, 49(8): 2567
- 5 Huang Chaowen, Ge Peng, Zhao Yongqing et al. *Rare Metal Materials and Engineering*[J], 2016, 45(1): 254 (in Chinese)
- 6 Buirette C, Huez J, Gey N et al. *Materials Science and Engineering A*[J], 2014, 618: 546
- 7 Semiatin S L, Soper J C, Sukonnik I M. *Scripta Metallurgica et Materialia*[J], 1994, 30(7): 951
- 8 Xu Hao, Sun Qianjiang, Wen Chao et al. *Rare Metal Materials and Engineering*[J], 2024, 53(1): 178 (in Chinese)
- 9 Nicholas E B, João Q D F, Benjamin D et al. *MATEC Web of Conferences*[J], 2020, 321: 12043
- 10 Wang Wensheng, Liu Xianghong, Zhao Xiaohua et al. *Titanium Industry Progress*[J], 2018, 35(4): 6 (in Chinese)
- 11 Shen G S, Furrer D. *Manufacturing of Aerospace Forgings*[J], 2000, 98: 189
- 12 Pilchak A L, Sargent G A, Semiatin S L. *Metallurgical and Materials Transactions A*[J], 2018, 49: 908
- 13 Semiatin S L. *Metallurgical and Materials Transactions A*[J], 2020, 51: 2593
- 14 Cheng Y H, Hsu C, Hung W Y. *Materialia*[J], 2020, 9: 100554
- 15 Zheng Z Y, Chai L J, Li Z H et al. *Materials Chemistry and Physics*[J], 2022, 276: 125318
- 16 Zheng Z, Chai L, Xiang K et al. *Acta Metallurgica Sinica (English Letters)*[J], 2020, 33: 12

## $\beta$ 退火处理 WSTi6421 钛合金中异常晶粒结构的表征与分析

王文盛<sup>1,2</sup>, 刘向宏<sup>2</sup>, 王海鹏<sup>1</sup>, 王凯旋<sup>2</sup>, 田彦文<sup>2</sup>, 严建川<sup>2</sup>, 李宇露<sup>2</sup>, 陈海生<sup>2</sup>

(1. 西北工业大学, 陕西 西安 710072)

(2. 西部超导材料科技股份有限公司, 陕西 西安 710018)

**摘要:** 研究了 $\beta$ 退火后的 WSTi6421 钛合金锻坯, 其组织中出現尺寸大于周边晶粒的异常粗大晶粒, 并形成了尺寸分布不均匀的异常晶粒组织。通过电子背散射衍射 (EBSD) 表征了 WSTi6421 钛合金锻坯上不同位置的锻态组织, 发现锻造形成的 $\beta$ 相立方织构的强度对 $\beta$ 退火后的晶粒尺寸起着重要作用。在 $T_{\beta}-50\text{ }^{\circ}\text{C}\sim T_{\beta}+10\text{ }^{\circ}\text{C}$ 温度区间内开展热处理实验并观察宏观及微观组织。结果表明, 锻造产生的 $\beta$ 相立方织构影响了次生 $\alpha$ 相的组织, 在经 $\beta$ 退火后进一步影响了退火过程中形成的 $\beta$ 相, 并且残余初生 $\alpha$ 相的钉扎效应对 $\beta$ 退火过程中 $\beta$ 晶粒的长大过程中起着重要作用。EBSD 分析结果表明, 锻造时形成的 $\beta$ 相立方织构的强度影响了 $\beta$ 退火后 $\beta$ 晶粒取向分布的差异。同时,  $\beta$ 退火过程中立方织构中大取向晶粒的演变表现出一定的选择性, 受到初生 $\alpha$ 相的钉扎效应、基体立方织构强度和 $\beta$ 晶粒与基体取向关系的多重影响。总体而言, 区域内织构强度越强, 大错位晶粒进行次生生长的可能性越小, 进一步加剧了 $\beta$ 退火后不同区域微观结构和晶粒取向分布的差异。

**关键词:** WSTi6421 钛合金;  $\beta$ 退火; 异常晶粒组织

**作者简介:** 王文盛, 男, 1982年生, 博士生, 西北工业大学, 陕西 西安 710072, 电话: 029-86514523, E-mail: wwsawy@163.com